WELDING RESEARCH

SUPPLEMENT TO THE *WELDING JOURNAL*, JANUARY 2024
Sponsored by the American Welding Society

Influence of Boron on Stress-Relief Cracking Susceptibility of T23 Steel

The effects of increasing boron content levels in the coarse grain heat-affected zone are analyzed

BY D. ZHANG AND X. WANG

Abstract

The effect of boron on stress-relief cracking (SRC) sensitivity in the coarse grain heat-affected zone (CGHAZ) of ASME SA213-T23 was studied by thermo-mechanical simulation. Then, the fracture mode, microstructure, carbide evolution, and boron segregation were observed by an optical microscope, a scanning electron microscope, a transmission electron microscope, and an electron probe microanalyzer. Finally, the mechanism of increasing boron content to improve SRC resistance was described. The results showed that when the boron content is lower than 0.0038 wt.-%, T23 steel is sensitive to SRC at 550–750°C (1022–1382°F), and the sensitive temperature range narrows as the boron content increases. When the boron content increases to 0.010 wt.-%, SRC can be eliminated. Moreover, boron addition did not improve grain boundary (GB) strength nor did it fundamentally change the fracture mode at high temperatures, but it significantly improved intergranular ductility. This is because the boron segregation at the GB inhibits the precipitation of $M_{23}C_6$ carbides, which reduces the void nucleation and alloy element depletion near the GB, thus significantly improving intergranular plasticity. The improvement of intergranular plasticity gives the grain sufficient time to deform and greatly improves the overall plasticity of the CGHAZ. As a result, the SRC resistance of the welded joint is significantly improved because the stress can be released through enough plastic deformation during postweld heat treatment or service.

Keywords

- T23 Steel
- Heat-Affected Zone
- Stress-Relief Cracking
- Boron Segregation
- Precipitation

Introduction

ASME SA-213 T23 steel (2.25Cr1.6WVNbBN) is a kind of low alloy heat-resistant steel with excellent high-temperature creep properties whose creep strength is twice that of traditional 2.25Cr1Mo steel (T22 steel) (Refs. 1, 2), and its creep performance below 600° (1112°F) can be compared with T/P91 steel (high-chromium martensitic heat-resistant steel) (Refs. 3, 4). The creep strength of T23 steel was improved through a multi-alloying design based on the T22 steel, and the carbon content was reduced to a low level of 0.04-0.10% to avoid welding cold cracks. Therefore, T23 steel was an ideal material for manufacturing critical heating surface components, such as water walls, superheaters, and reheaters of ultra-supercritical boilers (Refs. 5, 6). However, the application of T23 steel in China's supercritical power plants has been discontinued due to the failure of weld joints caused by reheat cracking (RC) (Refs. 7–12).

RC, also known as stress-relief cracking (SRC), occurs in the coarse grain heat-affected zone (CGHAZ) or weld metal (WM) under postweld heat treatment (PWHT) or service at high temperature, with the sensitive temperature range usually being between 500–750°C (932-1382°F) (Refs. 13–17). The occurrence of SRC usually results in sudden fracture without obvious plastic deformation, which is very dangerous during service. Generally, the main reason for SRC in low alloy high-strength steel is the relative weakening of grain boundaries (GBs), which is caused by precipitation inside grains leading to intragranular strengthening (Refs. 18, 19). However, our recent research (Ref. 20) shows the SRC of T23 steel is caused by the direct weakening of GBs, which is closely related to the precipitation of carbides at GBs. Further

https://doi.org/10.29391/2024/103.001

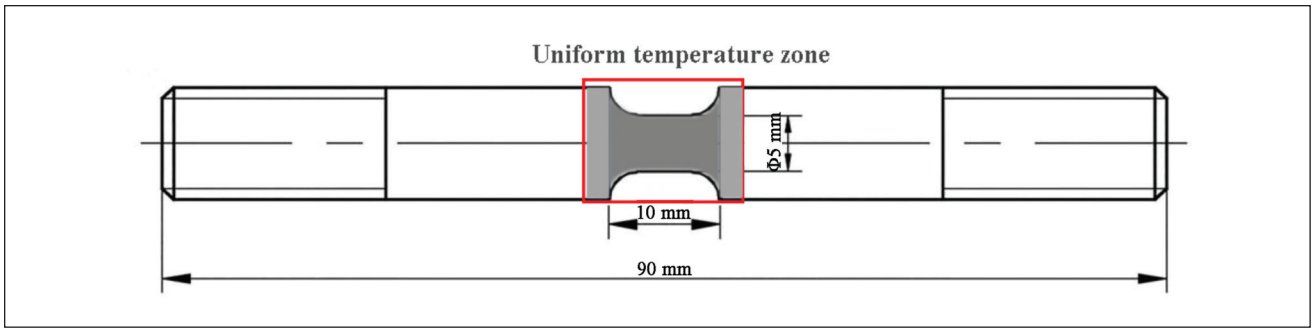

Fig. 1 — Schematic illustration of simulation and tensile sample.

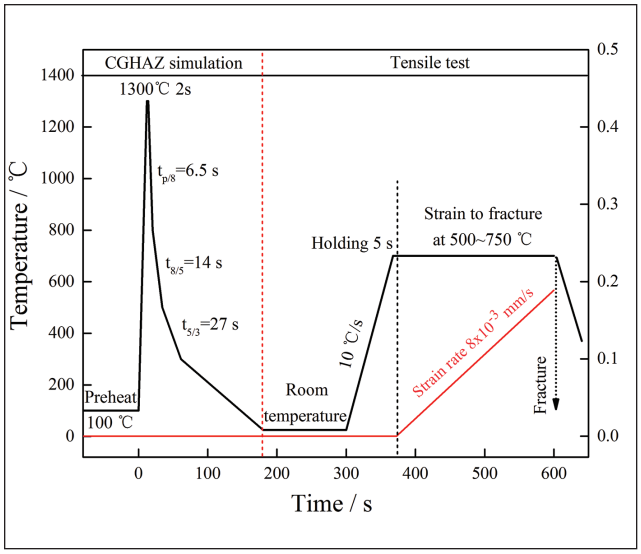

Fig. 2 — Schematic illustration of the thermal cycle curve.

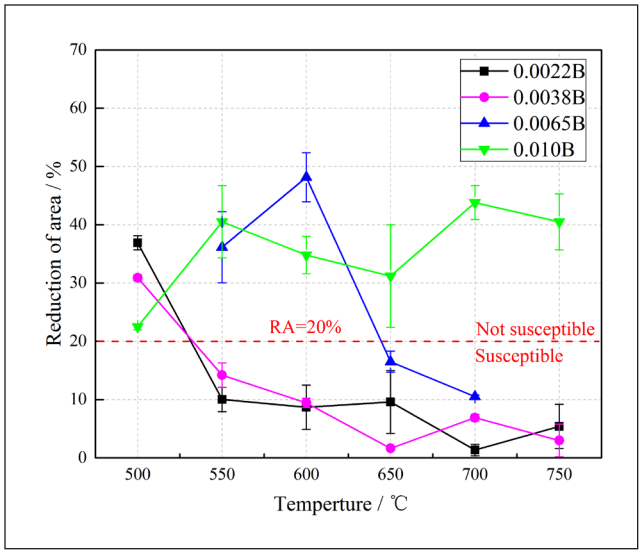

Fig. 3 — Effect of boron content on reduction of area of CGHAZs at different tensile temperatures.

research (Ref. 21) confirmed that reducing the carbon content of T23 steel can improve the SRC resistance by reducing the precipitation of GB carbides. This research not only further confirmed that GB carbides are the major factor affecting SRC but also provided a strategy for appropriately reducing carbon content to eliminate SRC in T23 steel. Unfortunately, to completely prevent SRC, the carbon content in T23 steel should be reduced to near the lower limit of 0.04% specified in the ASME standard, which may decrease the high-temperature strength and make it difficult to control the narrow carbon content in production. Therefore, it is necessary to find a new method to inhibit GB carbide precipitation.

Boron may be a potential element to suppress GB carbide precipitation and improve the SRC resistance of T23 steel. Shigesato et al. (Ref. 22) found that boron has a small atomic size, as well as minor solubility in steel, which will have a strong interaction with crystal defects (GBs, dislocations, vacancies, etc.). Boron is easy to segregate at the prior austenite grain boundaries (PAGBs) or sub-GBs, which affects the performance of steel. Briant et al. (Ref. 23) reported boron addition to Ni_3Al can enhance GB strength and greatly improve its plasticity and toughness. He et al. (Ref. 24) also discovered boron will segregate at PAGBs and affect the precipitation and coarsening behavior of the secondary phase at GBs. The above studies indicate that boron segregation at GBs has an impact on the precipitation and growth of the second-phase particle. However, can boron segregate in T23 steel CGHAZs? If so, can the precipitation of GB carbides be prevented? And how much boron needs to be added to completely eliminate SRC? To answer these questions is of great significance for the use of boron to improve SRC resistance in T23 steel.

In this study, four kinds of T23 steels with different boron content were selected to prepare CGHAZ samples by welding thermal cycle. SRC sensitivity was evaluated by an isothermal slow strain rate tensile test. Then, the fracture morphology, microstructure evolution, boron segregation, and its influence on GB carbide precipitation were studied. Finally, the mechanism of the effect of boron on the SRC sensitivity of T23 steel was discussed and the appropriate boron content for eliminating SRC was proposed.

Experimental

The investigated materials were T23 steels in the normalized (air cooling after holding at 1060±10°C [1940± 50°F] for 2 h) and tempered (furnace cooling after holding at 760±15°C

Table 1 — Chemical compositions of investigated T23 steel tubes (mass%)

No.	C	Si	Mn	Cr	Mo	V	Nb	Ti	W	B	N
0.0022B	0.076	0.24	0.36	2.16	0.09	0.24	0.030	0.004	1.50	0.0022	0.006
0.0038B	0.083	0.16	0.40	2.04	0.13	0.23	0.045	0.003	1.45	0.0038	0.003
0.0065B	0.085	0.17	0.35	2.16	0.11	0.25	0.038	0.027	1.56	0.0065	0.001
0.010B	0.091	0.17	0.35	2.18	0.12	0.25	0.038	0.030	1.57	0.010	0.002
ASME	0.04–	≤	0.10–	1.90–	0.05–	0.20–	0.02–	0.005–	1.45–	0.001–	≤
SA-213	0.10	0.50	0.60	2.60	0.30	0.30	0.08	0.060	1.75	0.006	0.015

[1400±59°F] for 1 h) condition with carbon content close to the upper limit of the ASME SA-213 standard. Its chemical compositions are listed in Table 1. According to boron content, the experimental materials were numbered 0.0022B, 0.0038B, 0.0065B, and 0.010B, respectively. Noteworthy, the boron content of 0.0065B and 0.010B exceeds the standard to explore the effect of increasing boron content on SRC.

The CGHAZ was simulated by the THERMECMASTOR-Z thermo mechanical simulator using a 90 mm- (3.54 in.-) long cylindrical specimen with threaded ends, as shown in Fig. 1. The simulated welding was gas tungsten arc welding with preheating at 100°C (212°F) and input energy of 25 kJ/cm, and the parameters are shown in Fig. 2 (CGHAZ simulation). After simulation, the specimens were heated to 500–750°C (the temperature range covered the service and PWHT of T23 steel) and maintained for 5 s then slowly strained at 0.5 mm/min (0.02 in/min) until fracture, as shown in Fig. 2 (Tensile test). The reduction of area (RA) was measured to assess the ductility that is related to SRC susceptibility. Two samples were tested for each temperature, and the average of RA was taken as the result. To understand the relationship between GB damage evolution and carbide precipitation during tensile, the 0.010B steel's CGHAZ was interrupted at 130 s under 700°C (1292°C) tensile condition.

The fracture surface was directly observed by a Quanta 400 scanning electron microscope (SEM) to determine the effect of boron content on fracture morphology. The longitudinal interface of the fracture sample was observed by the optical microscope ZEISS-Axio Observer 40MAT (OM) and the QUANTA-400 scanning electron microscope(SEM) to investigate features of the microstructure and crack propagation. The thin foil samples were made to observe the GB carbides precipitation and determine the type of carbides by a JEOL-2010 transmission electron microscope (TEM) with selected area electron diffraction (SAED). The depletion of alloying elements near the GB after carbide precipitation was measured by an INCA energy-dispersive x-ray spectrometer (EDS). Finally, the samples were prepared by grinding, polishing, and etching with 4% nitric acid alcohol solution. Then the distribution of B, C, and Cr in the CGHAZ was tested by the high-resolution EPMA-8050G electron probe microanalyzer (EPMA).

Results

Isothermal Slow Strain Rate Tensile Test

Figure 3 shows the RA of CGHAZs with different boron content at different tensile temperatures. For 0.0022B and 0.0038B steel, the RA decreased rapidly with increasing temperature and reached the minimum value of less than 5% at 650°C (1202°F) then maintained a small fluctuation when the temperature continued increasing. The RA of the 0.0065B steel's CGHAZ was significantly higher than that of the 0.0038 steel at 600°C, then it dropped sharply and reached the minimum value of about 10% at 700°C (1202°F), slightly higher than that of the 0.0022B and 0.0038B steel CGHAZs. For 0.010B steel, the RA was at a high level (>20%) in the whole tensile temperature range, especially at 650–750°C, much higher than the CGHAZs of the 0.0022B and 0.0038B steel CGHAZs (<10%). The results show that the increase of boron content can significantly expand the temperature range of ductile fracture under tensile stress and maintain a high RA at 650–750°C.

According to the standards formulated by Vinckier and Pense (Ref. 25), the SRC susceptibility of low alloy steel in engineering applications is evaluated as follows: 1) extremely susceptible, RA<5%; 2) highly susceptible, 5%<RA<10%; 3) slightly susceptible, 10%<RA<20%; 4) not sensitive, RA>20%. The SRC sensitivity of 0.0022B and 0.0038B is "slightly sensitive" at 550–600°C and "highly sensitive" at 650–750°C, while 0.0065B is "slightly sensitive" at 650–750°C, indicating a narrow range of sensitive temperature. Moreover, 0.010B is insensitive to SRC in the whole range of 500–750°C. This implies that the SRC sensitivity of T23 steel CGHAZs decrease with the increase of boron content, and SRC can be eliminated when the boron content reaches 0.01 wt.-%.

Figure 4A shows the stress-strain curve of T23 steel CGHAZs with different boron content at 700°C. With the increase of boron content, the high-temperature tensile strength of the CGHAZ first increases and then decreases. The tensile strain gradually increases, especially when the B content exceeds 0.0065%. Figure 4B compares the strain and strain energy density of T23 steel CGHAZs with different boron content at 700°C, where ε_u represents the strain at

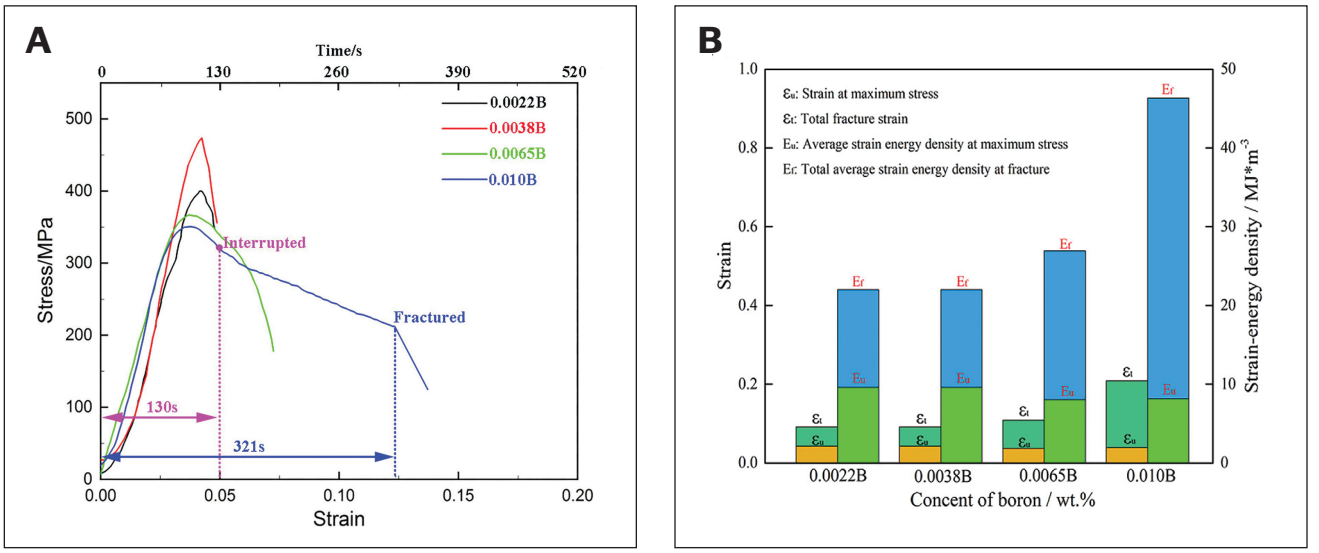

Fig. 4 — A — Stress-strain curves at 700°C of CGHAZs with different boron content; B — influence of boron content on the strain and strain energy density during a tensile test at 700°C.

the maximum stress and ε_f is the fracture strain. With the increase of boron content, ε_f gradually increases while ε_u is almost unchanged, indicating the increase of strain caused by the increase of boron content mainly occurs after reaching the maximum stress. Consequently, it can be concluded that the increase in fracture strain is mainly contributed to by the increase of nonuniform plastic deformation (neck shrinkage). E_u and E_f, respectively, represent the average strain energy density at maximum stress and the average strain energy density at fracture (toughness modulus). E_f increases gradually with the increase of boron content, which reflects the improvement of fracture ductility. However, E_u does not change significantly with the increase of boron content, indicating the increase of fracture strain energy density mainly comes from the increase of strain energy after reaching the maximum stress, which is consistent with the strain evolution characteristics shown in Fig. 4A.

The above analysis shows increasing boron content does not improve the tensile strength of CGHAZs in T23 steel, and the time to reach the maximum stress is almost the same for all experimental steels. The fracture can be divided into two stages: crack initiation and crack propagation. The crack initiation process often occurs before reaching the maximum stress (Ref. 26), while crack propagation occurs after reaching the maximum stress (Ref. 27). Therefore, it can be inferred that increasing boron content mainly enhances the ductility and fracture strain energy density of CGHAZs by increasing the crack propagation resistance. The following microscopic analysis will confirm this inference.

Fractography

Figure 5 shows the SEM images of fracture morphology at 700°C. The fracture of 0.0022B and 0.0038B steel CGHAZs shows typical intergranular brittle fracture with totally exposed crystal sugar-like grains (Figs. 5A and B). When the boron content increased to 0.0065%, the grain contour was still visible but became fuzzy and no longer clear (Fig. 5C). Many shallow fine and dense dimples were at the GB surface, indicating the intergranular plasticity has increased and the fracture mode had begun to change from brittle fracture to plastic fracture. Continuing to increase the boron content to 0.010%, the grain contour became more blurred (Fig. 5D), and the GB surface had many large and deep dimples (Fig. 5H), showing obvious plastic fracture characteristics. Generally, the fracture mode was still dominated by intergranular fracture with the increase of boron content from 0.0022 to 0.01 wt.-%, but the intergranular ductility gradually increased. In summary, the micromorphology changes of CGHAZs with different boron content were consistent with the evolution of macro plastic RA obtained in Fig. 3.

Microstructures of CGHAZs

Figures 6A–D show the OM images of CGHAZs of four steels with different boron content under as-welded conditions. The microstructures of CGHAZs were all a mixture of bainite and martensite, with the same prior austenite grain size of about 40–50 µm, indicating no change of microstructure by boron addition. After a tensile test at 700°C, the microstructure near the fracture is shown in Figs. 6E–H. For 0.0022B and 0.0038B steel CGHAZs, the grain deformation was still uniform equiaxed grains without obvious deformation (Figs. 6E and F), while the grain deformation increased for the 0.0065B steel CGHAZs and became larger for the 0.010B steel CGHAZs. Significantly, although the grain deformation was largest in 0.010B steel, secondary cracks still occurred only along the GBs, indicating the fracture mode was still mainly intergranular fracture. Additionally, no clear exposed grains were observed in 0.010B steel due to an increase in intergranular deformation capacity, making the inherent shape of grains with intergranular tear pits.

Figure 7 shows the SEM images near the fracture after tensile at 700°C. In the CGHAZs of 0.0022B and 0.0038B

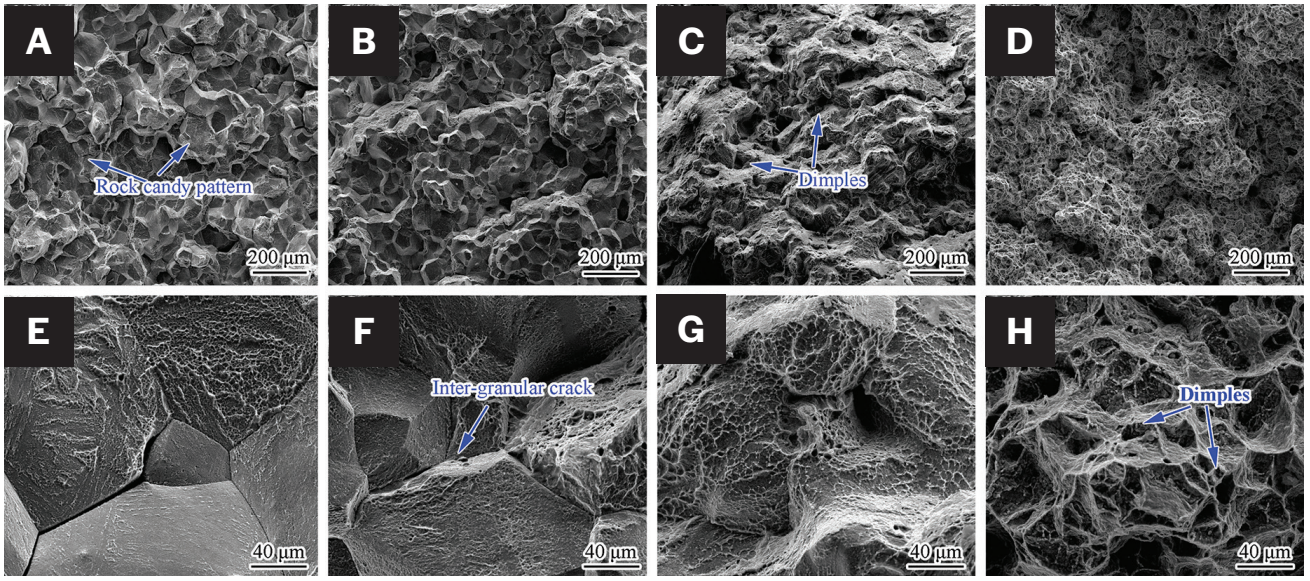

Fig. 5 — Micromorphology of fracture surfaces in CGHAZs after tensile tests at 700°C: A and E — 0.0022B steel; B and F — 0.0038B steel; C and G — 0.0065B steel; D and H — 0.010B steel.

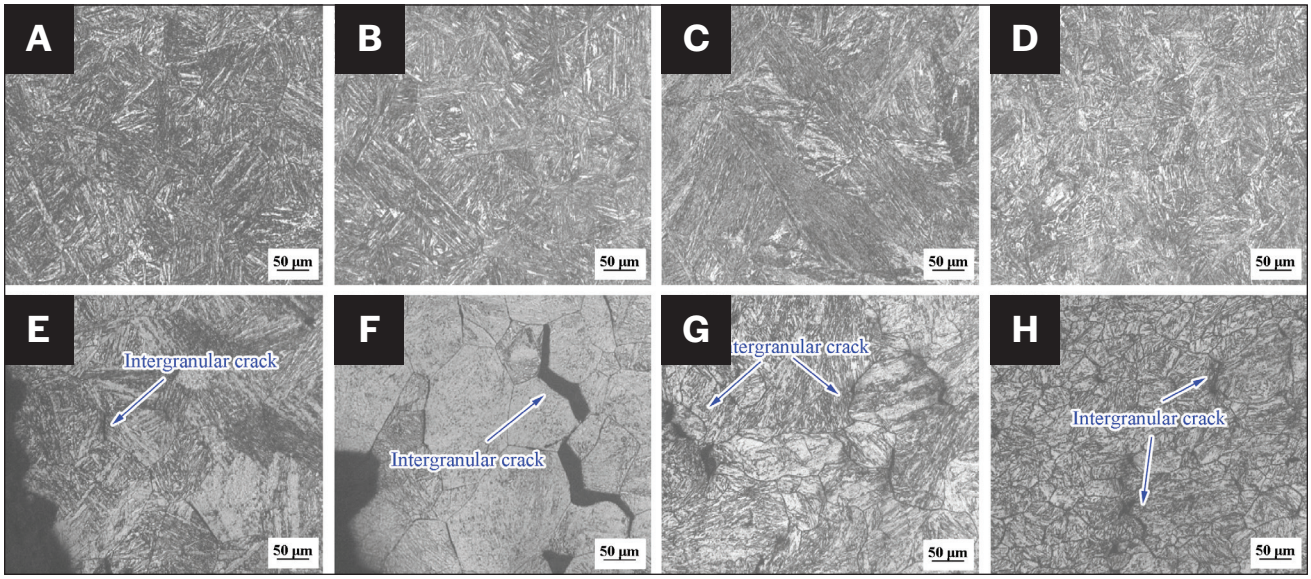

Fig. 6 — OM images of as-welded CGHAZs: A — 0.0022B steel; B — 0.0038B steel; C — 0.0065B steel; D — 0.010B steel, cross-section of CGHAZ near the fracture surface; E — 0.0022B steel; F — 0.0038B steel; G — 0.0065B steel; H — 0.010B steel.

steel (Figs. 7A and B), long and straight cracks or isolated microvoids were found in some GBs. In the 0.0065B steel CGHAZ (Fig. 7C), the length of the intergranular crack was shortened, and the edge became rough and saw-toothed, indicating the intergranular deformation was increasing. In the 0.010B steel's CGHAZ (Fig. 7D), the lengths of intergranular cracks were even shorter, and the microvoids were larger, and the edges of cracks and microvoids were very rough with more obvious intergranular tear marks, indicating the ability of intergranular deformation was further enhanced. As shown in Figs. 7E–H at high magnification, the CGHAZs with different boron content had similar intergranular fracture mechanisms.

The mechanism of fracture can be summarized as the generation of a single void at the GB and then aggregating into void chains with the increase of the number of voids, which finally developed into microcracks. This is consistent with the SRC formation mechanism revealed by Wang et al. (Ref. 21). Moreover, carbides precipitated at the GBs in the CGHAZs of all steels, providing more locations for nucleation of voids (Figs. 7F and G). However, for the 0.010B steel CGHAZs, the precipitation of carbides at the GB was obviously reduced. This shows that the addition of boron content reduces the amount of carbide precipitated at the GBs, thus inhibiting the generation of microvoids near the GBs.

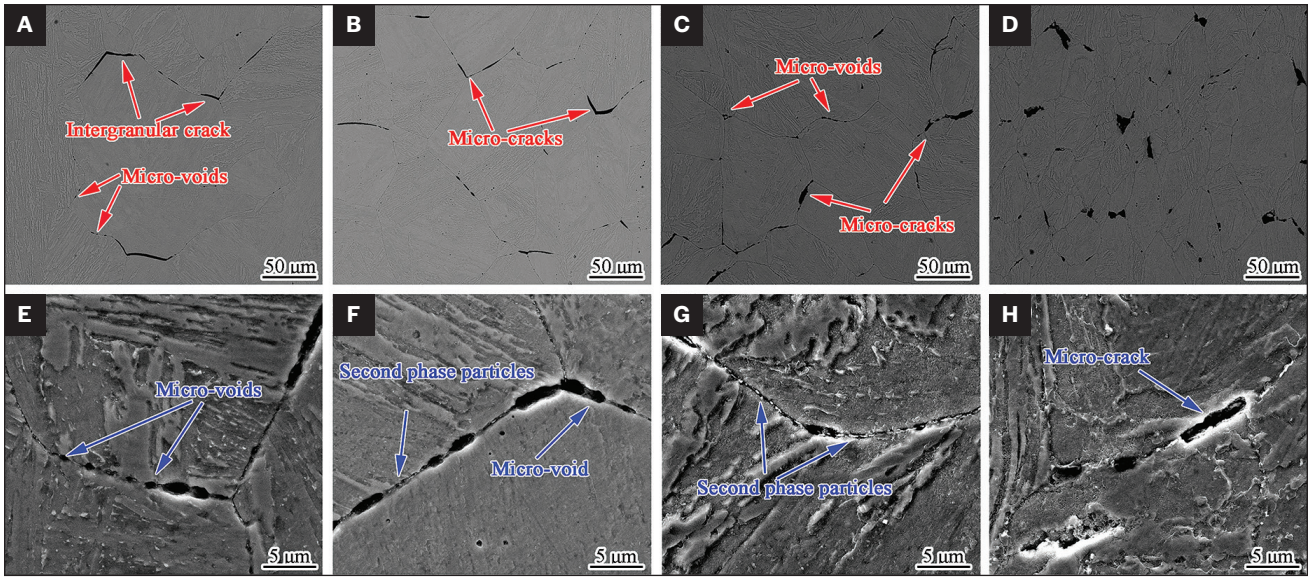

Fig. 7 — SEM images of the cross-section of CGHAZs near the fracture surface: A and E — 0.0022B steel; B and F — 0.0038B steel; C and G — 0.0065B steel; D and H — 0.010B steel.

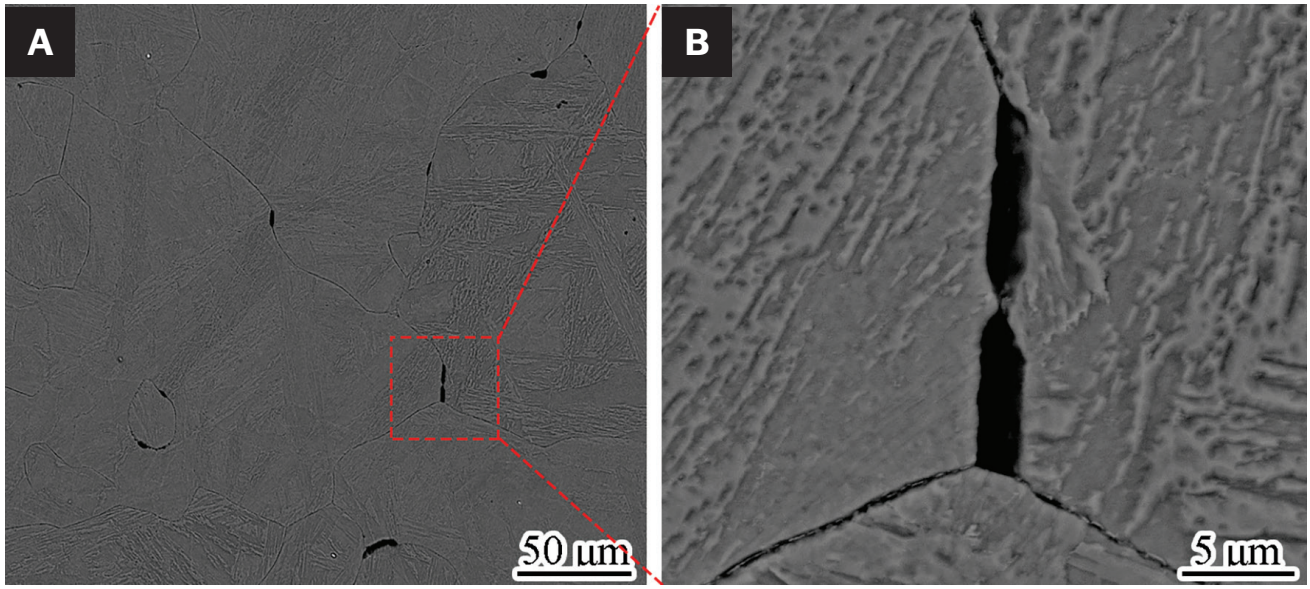

Fig. 8 — SEM images of 0.010B steel CGHAZ interrupted stretching for 130 s at 700°C.

Figure 8 shows the SEM images of the interrupted tensile test for 130 s at 700°C on the 0.010B steel CGHAZ sample. In comparison to Fig. 7D, the interrupted sample exhibits only a few microvoids and microcracks with significantly reduced sizes at the GBs (Fig. 8A), indicating that it is in the early stages of void nucleation and GB damage. It was further confirmed that GB damage caused by cavity aggregation was the main mechanism of intergranular fracture of the CGHAZs. Moreover, there was a small amount of carbide precipitation at the GBs, which further proves that the formation of voids is closely related to the amount of carbide precipitation.

Carbide Precipitation of CGHAZs

Figure 9 shows typical TEM images of carbides at GBs from thin foil samples at 700°C. A large number of short rod carbides with an average size of 247 nm were precipitated at the GB in the 0.0038B steel's CGHAZ (fractured at 122 s), while the number of carbides at the GB slightly increased in the 0.0065B steel's CGHAZ (fractured at 165 s), and the average size increased to 257 nm, which may be due to the increase of stretch time. It can be concluded that when boron content increases from 0.0038% to 0.0065 wt.-%, the precipitation rate of GB carbides in the CGHAZ is

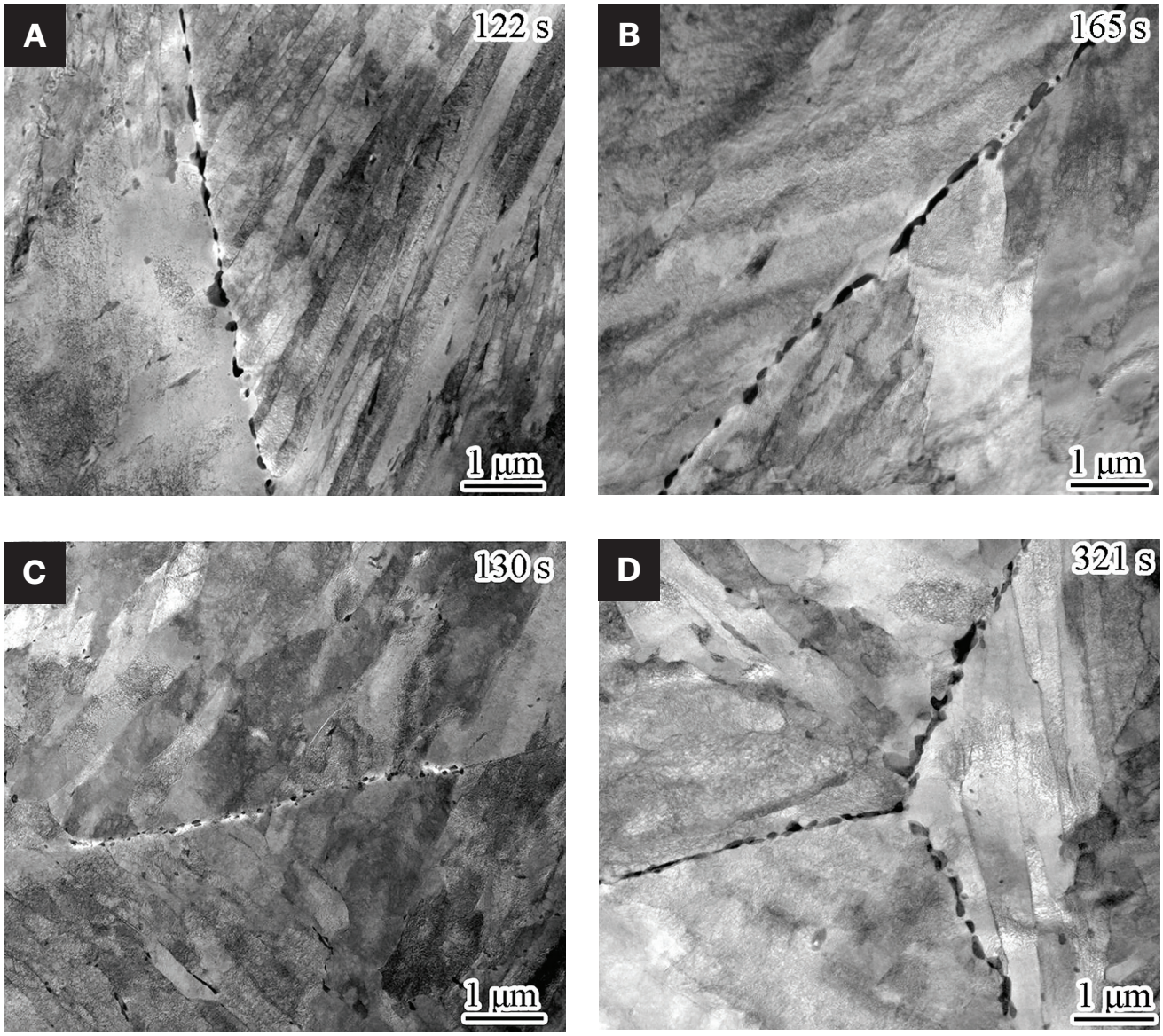

Fig. 9 — TEM images of carbides at GBs from thin foil samples of: A — 0.0038B fractured; B — 0.0065B fractured; C — 0.010B interrupted; D — 0.010B fractured.

still very fast, which seems unable to effectively prevent the precipitation of carbides. Figure 9C shows the TEM image of 0.010B steel's CGHAZ interrupted at 130 s. Compared with the 0.0038B and 0.0065B steel CGHAZs, the amount of carbide precipitation was significantly reduced, as was the size, which was only about 47 nm. Although the carbides continued to precipitate and grow up with the tensile time increases, the quantity and size were still slightly smaller than that of the 0.0038B steel's CGHAZ (Fig. 9D vs. Fig. 9A). The carbide evolution observations show that increasing the B content to 0.010% significantly delayed the precipitation of carbide in the GB. In addition, as shown in Fig. 9, the CGHAZ of steels with different boron content still retains obvious lath structure, with high-density dislocation and a small number of fine carbides precipitated in the grain during high-temperature tensile, indicating that the internal structure had only slightly recovered and the matrix had not been significantly softened. The matrix did not soften significantly.

Figure 10 shows the SAED analysis of carbides at GBs in 0.0038B steel CGHAZs at 700°C. The results show that they are $M_{23}C_6$ carbides. Abe et al. (Ref. 28) also found that boron addition in 9Cr steel can prevent the growth of $M_{23}C_6$, which is consistent with our observation in low-Cr T23 steel.

The above observations suggest that the increase of boron content from 0.0038 to 0.0065 wt.-% does not significantly delay the kinetics of carbide precipitation at GBs in T23 steel CGHAZs, and the corresponding RA increase is also little at 700°C. However, when the content of boron is increased to 0.010 wt.-%, the precipitation of carbide at the GBs is significantly delayed and the corresponding RA increases significantly. This phenomenon once again confirmed that GB carbide precipitation is the main factor leading to the

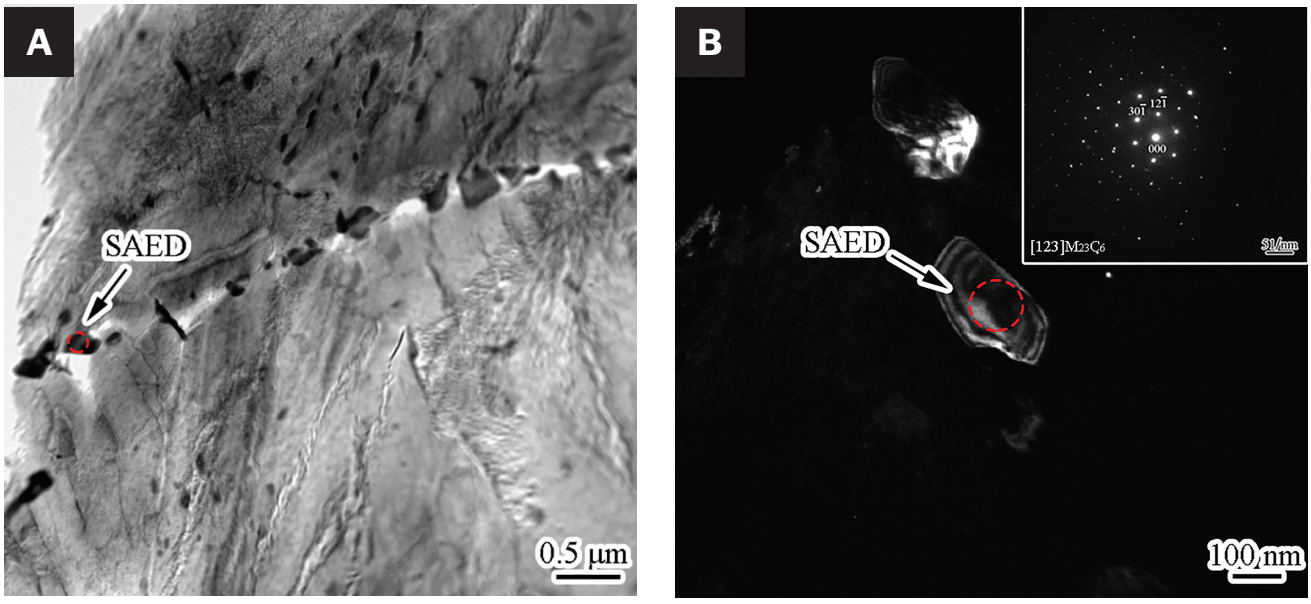

Fig. 10 — SAED of carbides at the grain boundaries from thin foil samples of 0.0038B steel CGHAZ fractured at 700°C: A — Electron diffraction region; B — dark field image.

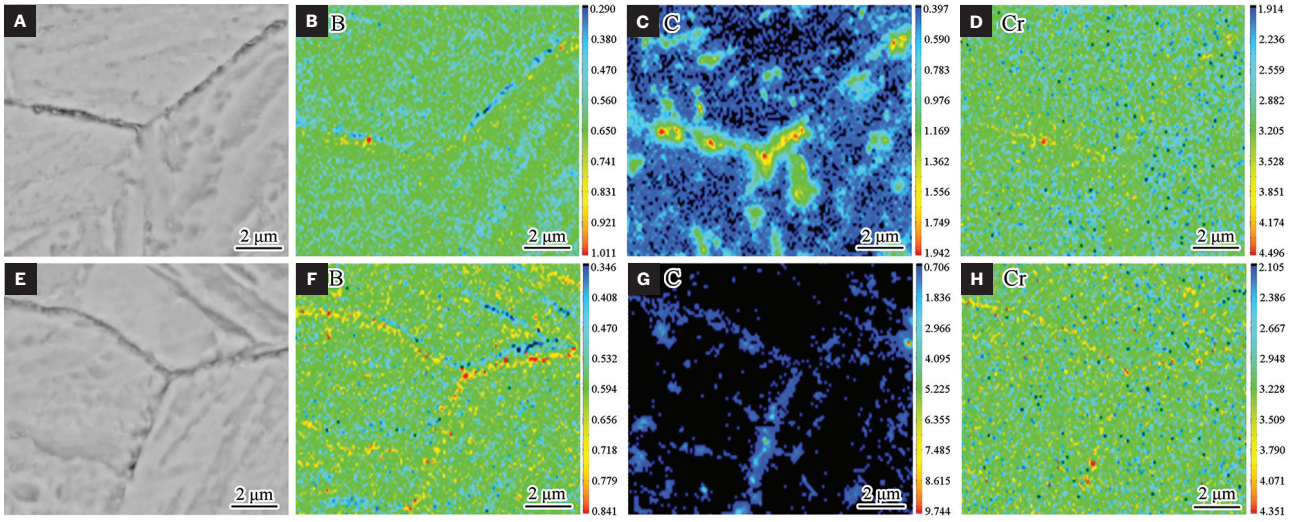

Fig. 11 — EPMA results of grain boundaries: 0.0038B steel: A — Scanning area; B — B, C — C; D — Cr, 0.010B steel: E — scanning area; F — B; G — C; H — Cr.

reduction of GB plasticity and the formation of SRC, which also indicates that the inhibition of SRC sensitivity by increasing boron content is closely related to the inhibition of GB carbide precipitation.

Boron Distribution in CGHAZs

Figure 11 shows the EPMA images of 0.0038 and 0.010B steel CGHAZs after stretching. The 0.010B steel CGHAZ sample was interrupted at 130 s, similar to the fracture time of the 0.0038 steel CGHAZ sample at 122 s for comparison at similar tensile time. Boron segregation is more serious at the GB in the 0.010B steel CGHAZ, while carbon segregation is more serious at the GB in the 0.0038B steel CGHAZ. Thus, combined with the difference in carbide precipitation shown in Fig. 9, it can be concluded that boron segregation at GBs can effectively prevent the aggregation of carbon at GBs, thus inhibiting carbide precipitation.

Depletion of Alloying Elements Near Grain Boundaries

Our previous studies (Refs. 20, 21) show that the precipitation of carbides in GBs during high-temperature tensile

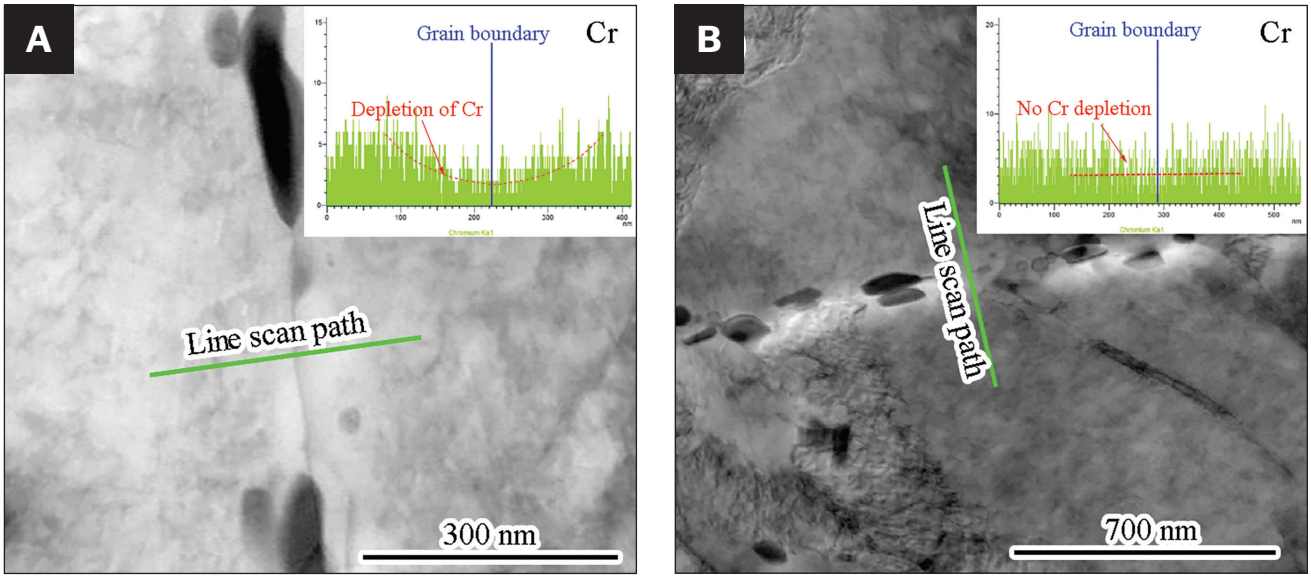

Fig. 12 — Depletion of Cr element near the GB in CGHAZ: A — 0.0038B steel fractured; B — 0.010B steel interrupted.

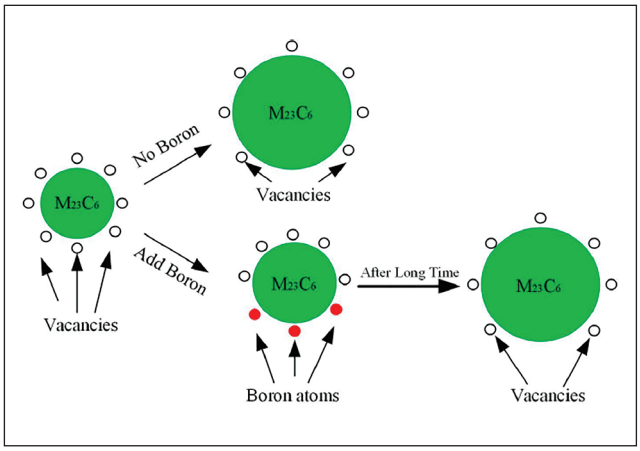

Fig. 13 — Mechanism of the boron inhibiting the growth of $M_{23}C_6$.

would lead to the depletion of alloying elements (e.g., Cr) in the vicinity of GBs. Figure 12 shows the EDS results of Cr distribution around the GBs in the 0.0038 and 0.010B steel CGHAZs after stretching. A wave trough, approximately 150 nm wide, formed near the GB in the CGHAZ of 0.0038B steel, indicating obvious depletion of Cr elements near the GB (Fig. 12A), while the depletion area significantly narrowed due to the reduction of carbide precipitation in the 0.010B steel's CGHAZ. The results show that the precipitation of GB carbides is inhibited with the increase of boron content, which causes the consumption of alloy element depletion to be reduced.

Discussion

Mechanism of Boron Inhibiting the Precipitation of $M_{23}C_6$ at the GB

A large amount of boron segregation at GBs affects the precipitation of $M_{23}C_6$. Generally, the precipitation of $M_{23}C_6$ at GBs includes nucleation and growth, which is driven by the decrease of total free energy (Ref. 29). During the nucleation of $M_{23}C_6$, a lot of vacancies and crystal defects around GBs will be occupied, reducing the phase transition free energy of new phase nucleation and inhibiting the formation of a new phase. Therefore, it is more difficult to form the nucleation core of the $M_{23}C_6$ phase in the high-boron alloy system.

According to the Ostwald ripening theory, the precipitation phase particles need to adjust the local volume change around the particles during the phase growth process, which can be used to explain why boron can prevent the growth of $M_{23}C_6$. Figure 13 shows the mechanism of the boron inhibiting the growth of $M_{23}C_6$. Because the volume occupied by the carbide with unit mass is larger than that occupied by the matrix with unit mass, when a small carbide is produced in the matrix, the carbon atom will occupy the gap position in the matrix, thus creating a vacancy at the carbide interface. This vacancy then migrated to the growing carbide interface through the matrix to adapt to local volume changes (Ref. 30). However, boron segregation will occupy vacancies near the carbides interface, which makes it difficult to adapt to the volume changes around the carbide, thus inhibiting the growth of the carbide and achieving the effect of refining the size of the carbide. The carbide will continue to grow after a longer period of heat preservation.

In brief, increasing boron content can prevent the precipitation and growth of $M_{23}C_6$ at GBs during reheating. Therefore, under similar tensile time, it can be observed that the $M_{23}C_6$

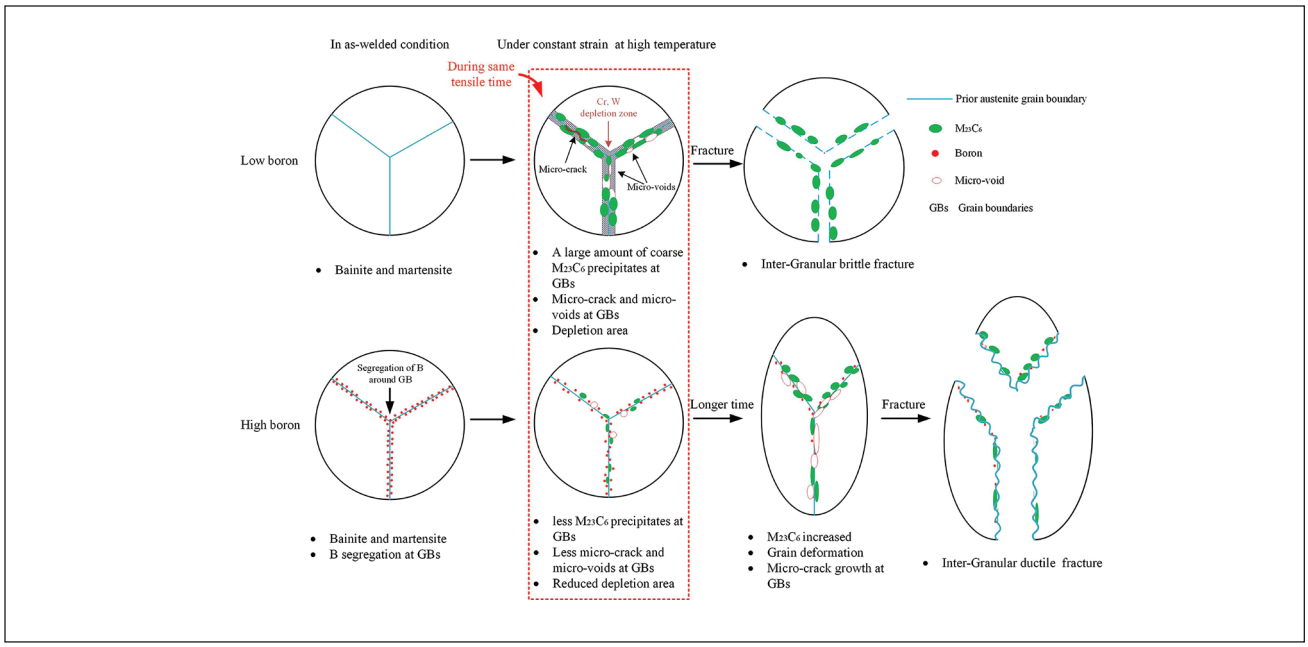

Fig. 14 — Influence mechanism of boron on SRC sensitivity in T23 steel.

precipitation at GBs in 0.010B steel CGHAZs is significantly less than that of 0.0038B steel, and the coarsening rate is also significantly reduced.

Mechanism of Eliminating SRC by Increasing Boron Content

The high-temperature tensile tests showed that with the increase of boron content, the hot ductility of the CGHAZ gradually increases, especially at 650–750°C. The fracture mode changed from intergranular brittle fracture to intergranular ductile fracture, and the SRC resistance increased. When the boron content is increased to 0.010 wt.-%, SRC can be eliminated within a wide range of 500–750°C. The boron content of 0.010 wt.-% exceeds the upper limit of the ASME standard for T23 steel (0.001–0.006 wt.-%). Therefore, from the perspective of eliminating SRC, it is necessary to consider appropriately increasing the upper limit of boron content to improve SRC resistance.

Based on the stress-strain curve (Fig. 4) and the characteristics of intergranular fractures (Fig. 5), it can be determined that minor boron addition can improve intergranular plasticity. Li et al. and Wang et al. (Refs. 20. 21) reported that the SRC of T23 steel is mainly caused by a large amount of $M_{23}C_6$ precipitated at GBs to promote the generation of microvoids and lead to alloy elements depletion at GBs. The addition of boron can prevent the precipitation of $M_{23}C_6$ at GBs, thus delaying the nucleation and growth of microvoids, inhibiting the formation of microcracks and ultimately improving GB plasticity. At the same time, the grains also have sufficient time to deform. The combined effect of these two aspects greatly improves the overall plasticity of CGHAZs. Therefore, the weld joints have sufficient deformation to release the residual stress without damage during PWHT or service. Moreover, the effect of boron on GB plasticity is not obvious when the tensile temperature is lower than 550°C. This is because the boron segregation at GBs is weakened at a lower temperature, and the role of boron is not utilized due to the lesser precipitation of $M_{23}C_6$.

Synthesizing the above analysis, the influence mechanism of boron on SRC sensitivity in T23 steel CGHAZs can be summarized as in Fig. 14. For low boron steel, a large amount of $M_{23}C_6$ precipitates and accumulates at the GB, resulting in the depletion area of the alloy element near the GB and promoting the nucleation of many microvoids at the GB. Then, the microvoids will grow and aggregate to form microcracks, which eventually quickly expand to cause intergranular fracture. For high boron steel, a large amount of boron preferentially segregates at PAGBs in as-welded conditions, so the carbide precipitation is delayed during high-temperature tensile. The main stage of crack initiation is before the stress reaches the maximum, and the time for low and high boron steels to reach the maximum stress is similar (Fig. 4). Accordingly, the smaller amount of $M_{23}C_6$ precipitated at the GB decreases the chance of void nucleation and then enhances GB plasticity to avoid early GB damage. With the extension of high-temperature tensile time, although the GB carbides continue to precipitate and grow up, the alloying element depletion caused by their precipitation can be timely supplemented through diffusion, thus increasing the resistance to microvoids and microcracks expansion, finally enhancing the ability of intergranular plastic deformation. In conclusion, increasing boron content can improve the SRC resistance of T23 steel.

Conclusions

1. For T23 steel with carbon content close to the upper limit of ASME standards, when the B content is lower than 0.0038 wt.-%, it is sensitive to SRC at 550–750°C. With the increase of B content, fracture ductility increases at tensile temperatures above 550°C, and the SRC sensitive temperature range is reduced. When the boron content increases to

0.010 wt.-%, SRC can be completely avoided in the service or PWHT temperature range of 500–750°C.

2. Increasing boron content does not increase the intergranular strength of CGHAZs nor does it fundamentally change the fracture mode at high temperature from intergranular fracture to transgranular fracture, but it significantly improves intergranular ductility.

3. The main reason for boron to improve SRC resistance at high temperatures is that boron segregation delays the precipitation and growth of GB $M_{23}C_6$, inhibits void nucleation and alloy element depletion near GBs, and, finally, significantly improves intergranular plasticity.

4. The addition of boron can improve the plasticity of GBs, thus allowing sufficient time for deformation in grains, greatly improving the overall plasticity of CGHAZs. Therefore, the welded joint can release stress during the tensile process through plastic deformation without damage, thereby significantly improving SRC resistance.

Acknowledgments

The authors would like to express their gratitude for projects supported by the National Natural Science Foundation of China (52174370 and 51574181) and Key Research and Development Project of Hubei Province (2021BAA058).

References

1. Masuyama, F., Yokoyama, T., Sawaragi, Y., and Iseda, A. 1994. Development of a tungsten-strengthened low-alloy steel with improved weldability. *Materials for Advanced Power Engineering Part 1*: 173–181.

2. Miyata, K., Igarashi, M., and Sawaragi, Y. 1999. Effect of trace elements on creep properties of 0.06c-2.25cr-1.6w-0.1mo-0.25v-0.05nb steel. *ISIJ INT* 39: 947–954.

3. Bendick, W., Gabrel, J., Vaillant, J., and Vandenberghe, B. 2004. Properties and workability of new creep strength enhanced steels as known grades 23, 24, 911 and 92. *ASME/JSME Pressure Vessels and Piping Conference*: 5–10.

4. Vaillant, J. C., Vandenberghe, B., Hahn, B., et al. 2008. T/P23, 24, 911 and 92: New grades for advanced coal-fired power plants—Properties and experience. *International Journal of Pressure Vessels and Piping* 85(1): 38–46.

5. Bendick, W., Gabrel, J., Hahn, B., et al. 2007. New low alloy heat resistant ferritic steels T/P23 and T/P24 for power plant application. *International Journal of Pressure Vessels and Piping* 84(1-2): 1–20.

6. DuPont, J. N., Siefert, J. A., and Shingledecker, J. P. 2017. Microstructural evolution and mechanical properties of grades 23 and 24 creep strength enhanced ferritic steels. *International Materials Reviews* 62(1): 32–56.

7. Ren, Y. B., Wang, W., and Ping, S. B. 2016. Failure analysis of T23/TP347H dissimilar steel welded tube joint for high temperature reheater. *Heat Treatment of Metals* 41: 199–203.

8. Long, H. G., Long, Y., and Chen, H. D. 2011. Mechanism of T23/12Cr1MoV dissimilar steel welding failure in high temperature reheater. *Electric Power* 44: 70–73.

9. Nawrocki, J. G., Dupont, J.N., Robino, C.V., and Marder, A.R. 2000. The stress-relief cracking susceptibility of a new ferritic steel — Part 1: Single-pass heat-affected zone simulations. *Welding Journal* 79: 355–362.

10. Hooge, A., and Vekeman, J. 2005. New generation 21/4Cr steels T/P 23 and T/P 24 weldability and high temperature properties. *Weld World* 49: 75–93.

11. Wang, X., Zhu, D., Hu, L., et al. 2015. Short term failure analysis of T23 steel joint of water wall of 1000MW tower furnace. *Chinese Journal of Electrical Engineering* (S1): 154–161.

12. Long, H. G., Long, Y., and Chen, H. D. 2011. Failure mechanism of T23/12Cr1MoV dissimilar steel weld of high-temperature reheater. *China Power* (05): 70–73.

13. Dhooge, A., and Vinckier, A. 1987. Reheat cracking — A review of recent studies. *International Journal of Pressure Vessels and Piping* 27: 239–269.

14. Yu, Z., Zhang, J., Wang, H., Zhou, R., and Yuan, Y. 2017. Mechanism of stress relief cracking in a granular bainitic steel. *Acta Metallurgica Sinica (English Letters)* 30: 156–163.

15. Chen, Z. B., Lv, Y. S., Shi, W., Qi, Q. Y., Wang, H. B., and Xing, J. T. 2016. Research progress on reheat crack of welded joint of low alloy heat resistant steel. *Welding* 12: 21–27.

16. Dhooge, A., Dolby, R. E., Sebille, J., Steinmetz, R., and Vinckier, A. G. 1978. A review of work related to reheat cracking in nuclear reactor pressure vessel steels. *Int. J. Pres. Ves. Pip* 6: 329–409.

17. Francis, J. A., Mazur, W., and Bhadeshia, H. K. D. H. 2006. Review Type IV cracking in ferritic power plant steels. *Mater. Sci. Tech* 22: 1387–1395.

18. McCullough, C., and Baker, A. J. 1991. The role of grain boundary migration in reheat cracking. *Acta Metallurgica et Materialia* 39(12): 3217–3225.

19. Welding Society of China Society of Mechanical Engineering. 2012. Machinery Industry Press: *Welding Manual* 2(3): 146–149.

20. Li, Y., Wang, X., Wang, J., and Chen, A. 2019. Stress-relief cracking mechanism in simulated coarse-grained heat-affected zone of T23 steel. *J Mater. Process. Tech* 266: 73–81.

21. Wang, X., Zhang, D. D., Yong, L., and Wei, Z. 2022. Effect of carbon on stress-relief cracking susceptibility of T23 steel. *Welding Journal* 10: 253s–261s.

22. Shigesato, G., Fujishiro, T., and Hara, T. 2014. Grain boundary segregation behavior of boron in low-alloy steel. *Metallurgical and Materials Transactions A* 45: 1876–1882

23. Briant, C. L., and Taub, A. I. 1988. Grain boundary segregation of boron and sulfur and its effect on ductility in rapidly solidified Ni-base L12 compounds. *Acta Metallurgica* 36: 2761–2770.

24. He, X. L., Chu, Y. Y., Chang, H. L., Yu, T. S., Li, C. P., and Yin, H. K. 1977. The distribution of boron in steel. *Acta Metallurgica Sinica* 13: 235–245.

25. Vinckier, A. G., and Pense, A.W. 1974. *WRC bulletin. A review of underclad cracking in pressure-vessel components*. New York: Welding Research Council

26. Ravi-Chandar, K., and Knauss, W. G. 1984. An experimental investigation into dynamic fracture: I. Crack initiation and arrest. *International Journal of Fracture* 25: 247–262.

27. Ha, Y. D., and Bobar, F. 2010. Studies of dynamic crack propagation and crack branching with peridynamics. *International Journal of Fracture* 162: 229–244.

28. Abe, F. 2008. Effect of boron on creep deformation behavior and microstructure evolution in 9% Cr steel at 650°C. *International Journal of Materials Research* 99: 387–394.

29. Yong, Q. L. 2006. *The second phase in iron and steel materials.* Metallurgical Industry Press.

30. Anderson, T. L. 2017. *Fracture mechanics: Fundamentals and applications*. CRC Press.

DONGDONG ZHANG and **XUE WANG** (*wangxue2011@whu.edu.cn*) are with the School of Power and Mechanics, Wuhan University, Wuhan, China.